

Thermal failure mechanism and failure threshold of SiC particle reinforced metal matrix composites induced by laser beam

Y.C. Zhou^{a,*}, S.G. Long^a, Y.W. Liu^b

^a *Institute of Fundamental Mechanics and Material Engineering, Xiangtan University, Xiangtan, Hunan 411105, China*

^b *Department of Engineering Mechanics, Hunan University, Changsha, Hunan 410082, China*

Received 8 June 2002; received in revised form 1 September 2002

Abstract

The failure of particulate-reinforced metal matrix composites (MMCs) induced by laser beam thermal shock is experimentally and theoretically studied. It is found that the initial crack occurs in the notched-tip region, wherein the initial crack is induced by void nucleation, growth and subsequent coalescence in the matrix materials or interface separation. However, crack propagation occurs by fracture of the SiC particle and it is much different from the crack initiation mechanism. The damage threshold and complete failure threshold can be described by a plane of applied mechanical load σ_{\max} , and laser beam energy density E_J . A theoretical model is proposed to explain the damage/failure mechanism and to calculate the damage threshold and complete failure threshold. This model is based on the idea of stress transfer between a reinforced-particle and the matrix, as well as the calculation of the applied mechanical stress intensity factor and local thermal stress intensity factor. In order to check the validity of the theoretical model, the finite element simulations are carried out for the temperature field induced by laser heating, the stress fields induced by the combined laser heating and applied mechanical tensile load. Both the theoretical model and the finite element simulation can explain the experimental phenomenon. The theoretical model can predict the damage threshold and failure threshold. The failure of MMCs induced by laser thermal shock and applied mechanical load is non-linear.

© 2002 Elsevier Ltd. All rights reserved.

Keywords: Thermal failure; Particulate-reinforced metal matrix composites; Laser beam; Damage and failure mechanism; Damage and failure threshold

1. Introduction

Metal matrix composites (MMCs) are excellent candidates for structural components in the aerospace and automotive industries due to their high specific modulus, strength, and thermal stability (Llorca, 2002; Tjong and Ma, 2000). MMCs can be fabricated by standard techniques,

* Corresponding author. Tel.: +86-732-8293586; fax: +86-732-8292468.

E-mail addresses: zhouyc@xtu.edu.cn, yichunzhou@hotmail.com (Y.C. Zhou).

considerably reducing the manufacturing cost and providing a good balance between price and mechanical properties. Many papers have been devoted to the preparation, micro-structure, corrosion behavior, creep properties and fatigue properties of MMCs (Llorca, 2002; Tjong and Ma, 2000; Shi et al., 2001; Rabiei et al., 2000; Podlesak et al., 2000; Li and Ellyin, 1999). However, the structural components applied for the aerospace and automotive industries are often subjected to severe thermal loads produced by aerodynamic heating, laser irradiation and localized intense fire (Zhou et al., 1997; Berlin et al., 1992). Thermal shock will lead to intense thermal stress concentration in the components containing cracks and various kinds of defects, especially in the components of ceramic-reinforced MMCs because of thermal-elastic mismatch between the metal and ceramic. Such a concentration of thermal stresses around defects often results in catastrophic failure of components. To solve the problem mentioned above a general methodology for durability and damage analysis of these structures exposed to intense thermal shock and mechanical load is required to be developed by establishment of a materials property database at elevated temperatures, such as fracture mechanics solution technique, for determining the thermal stress intensity factor, and studies of fracture behavior etc. Therefore, it is necessary to study the properties of MMCs subjected to the combined loads of thermal shock and mechanical loads for these composites used in a thermal environment. Usually the thermal shock is generally produced by a quenching method. However, a laser beam irradiating the specimen, was used to produce the thermal shock by radiating the specimen being studied. In this new method, the rate of temperature rise can easily be controlled by adjusting the laser intensity density and laser irradiated region. In this work, the thermal failure mechanism and failure threshold of particulate-reinforced MMCs have been experimentally and theoretically investigated. In this experimental study, the thermal load is simulated with laser thermal shock, as it is more convenient than any other heating method.

2. Experimental procedure

2.1. Laser beam thermal shock

Thermal shock was generated by an incident laser beam, which impinges normally to a single-edge notched specimen. The diagnostics of the laser parameters provided a traditional monitoring of the laser beam characteristics, such as energy, temporal, and spatial shapes (Zhou et al., 1999). A photoelectric cell with a response time of less than 1.0 ns was used to measure the temporal shape of the laser beam, while the spatial shape of the laser intensity was detected by a charge-coupled device sensor. The energy of the laser beam ranged from 1 to 40 J with a power intensity density of the order of 1.0×10^4 – 18.0×10^4 W/cm². It was a single pulse Nd:glass laser with the wavelength of 1.06 μ m. The normalized intensity I/I_{\max} vs time and space coordinates r/a are shown in Figs. 1 and 2, where r and a are the radial distance and the radius of the laser spot, respectively. The pulsed Nd:glass laser beam with the full width at half of the maximum (FWHM) of 250 μ s was used to generate the thermal shock. The spatial distribution of the laser intensity is non-Gaussian but is roughly uniform within the laser-irradiated region and declines very sharply toward the edge where the laser spot terminates. For the convenience of numerical analysis, the laser intensity I is approximated by

$$I = I_{\max} e^{-\alpha_1 t} (1 - e^{-\beta_1 t}) f(r) = I_{\max} g(t) f(r) \quad (1)$$

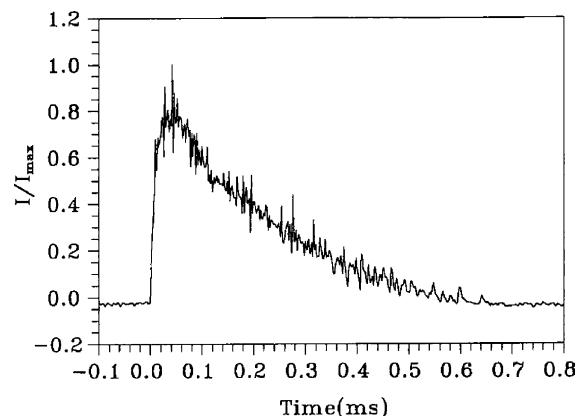


Fig. 1. Temporal shape of Nd:glass pulsed laser intensity with a FWHM of 250 μ s.

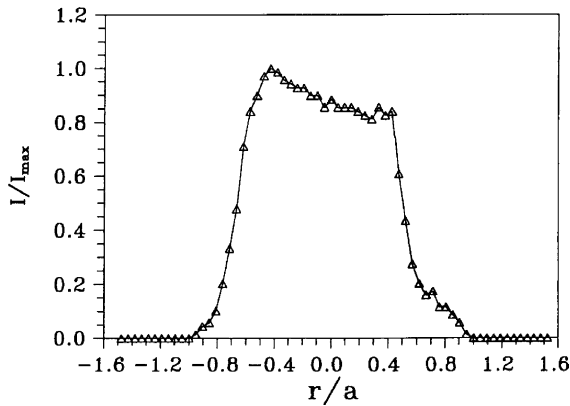


Fig. 2. Spatial shape of Nd:glass pulsed laser intensity.

where α_1 and β_1 are experimentally determined and equal to 1.5×10^4 and $18.0 \times 10^4 \text{ s}^{-1}$ respectively. Therefore, the laser energy is $E_J = \beta_1 \pi a^2 I_{\max} / \alpha_1 (\alpha_1 + \beta_1)$

$$f(r) = \begin{cases} 1 & \text{if } 0 < r < a \\ 0 & \text{if } a < r < \infty \end{cases} \quad (2)$$

In addition, the spatial distribution of the laser beam has to be accounted for.

2.2. Specimen and loading

SiC particulate/6061 Al composite was chosen as a model MMCs system for this study. The composite with 15 wt.% SiC was fabricated by melt casting route, and as-cast ingots of the composite were subsequently extruded. SiC particulates with an average size of 10 μm were distributed uniformly throughout the aluminum alloy matrix. This uniformity of the micro-structure is believed to be responsible for the isotropic nature of mechanical properties. Specimens cut from a hot-pressed billet and single-edge notched with the dimension of $20 \times 8 \times 0.3 \text{ mm}^3$, were installed on a static tensile machine during the test. Before the laser beam was applied the static tensile stress was already loaded on the sample. The thermal damage and failure were induced by both laser thermal shock and the loaded static tensile stress. Fig. 3 is a schematic of the specimen configuration and dimensions with the geometrical parameters listed in Table 1. The starter U-shape notch shown here was made with an electric discharge machine. The

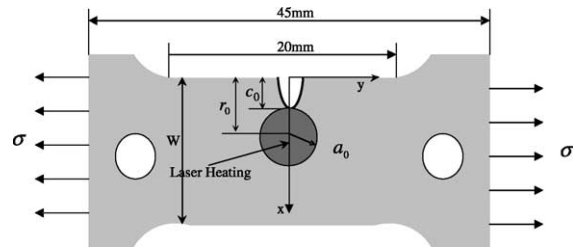


Fig. 3. Schematic of the specimen configuration and dimensions.

Table 1
Geometrical parameters

| | |
|------------|-----|
| w (mm) | 8.0 |
| c_0 (mm) | 0.5 |
| r_0 (mm) | 4.0 |
| a_0 (mm) | 2.5 |
| h (mm) | 0.3 |

polished rear surface of the notched specimen was examined by both optical microscopy and scanning electron microscopy (SEM), while the front surface was irradiated by the laser beam in order to heat the notched-tip region. As is well known, the maximum stress should locate at the notched-tip and the coefficient of stress concentration is usually $\alpha_\sigma = 3.2$ for the U-like notch (Zhou et al., 2001a,b). Therefore, the maximum stress at the tip of the notch is $\sigma_{\max} = \alpha_\sigma \sigma$. During the experiment, the samples were subjected to different coupled loads of applied mechanical load σ and laser thermal load (σ_{\max}, E_J) , where E_J is the energy density of incident laser beam. As we will know from the later discussion, the laser thermal shock will cause the temperature rise and thermal stress in the specimen and, hence, the thermal load can be described by the laser energy density E_J .

3. Experimental results

3.1. Damage mechanism

When the coupled loads (σ_{\max}, E_J) were low (i.e. σ_{\max} and E_J were lower than the threshold ones), there was no damage phenomena observed in the

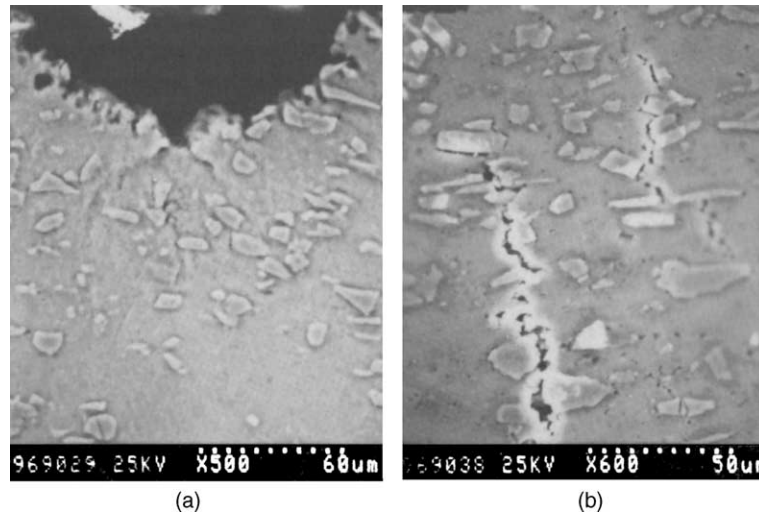


Fig. 4. Damage characteristics: (a) SEM of micro-voids in the notched-tip region and (b) radial cracking showing voids in matrix and the separation between SiC particle and matrix.

specimen. However, as the coupled loads (σ_{\max} , E_J) reached the thresholds, damage phenomena were began to observe at the notch-tip first by SEM. Fig. 4(a) shows the typical SEM image of micro-voids in the notched-tip region. It is observed that the voids occur in the form of interfacial debonding at the particle/matrix interface, whereas the micro-cracks occur in both the matrix and the interface. It is very interesting to note here that, the reinforcement SiC particle at the crack tip does not fracture but resists crack propagation. In order to clarify the initial damage behavior of the composite induced by laser beam heating, the laser beam irradiated region was deviated from the notched-tip region. In this case, the radial crack appeared around the periphery of the laser beam irradiated region, as shown in Fig. 4(b). The radial crack was initiated by the void nucleation and growth within the matrix, as well as decohesion at the particle/matrix interface. A little fracture SiC particulate could be observed, as shown in Fig. 4(b). It can be concluded that the initial damage is produced by separation at the SiC particle-matrix interface or by void nucleation and the following growth in the matrix. The onset and progression of this ductile matrix failure is promoted by the development of local plastic strains and hydrostatic stresses during the coupled loading. The initial

damage is similar to a fatigue fracture behavior (Davidson, 1991).

3.2. Crack propagation

When the thermal shock and mechanical loads (σ_{\max} , E_J) were gradually increased, the damage became more and more serious. Once the coupled loads (σ_{\max} , E_J) were up to threshold, the micro-cracks formed in the notched region grew into macroscopic cracks. The typical microscopic feature of a macro-crack tip is shown in Fig. 5. As shown in the figure, the fracture of the reinforcement SiC particle is the dominant damage mechanism for macro-crack propagation. The reinforcements were broken by cracks perpendicular to the loading axis, and the fraction of broken reinforcements increased near the crack tip zone. It should be pointed out that the characteristics of the SEMs, shown in Fig. 5, for crack propagation are very different from those shown in Fig. 4 for damage initiation. It is very interesting that although the particles were broken near the macro-crack tip region, there was no damage in the matrix and at the particle/matrix interfaces.

Generally, the microscopic failure characteristics of MMCs, induced by the coupled loads, are in three forms: matrix failure caused by void nucle-

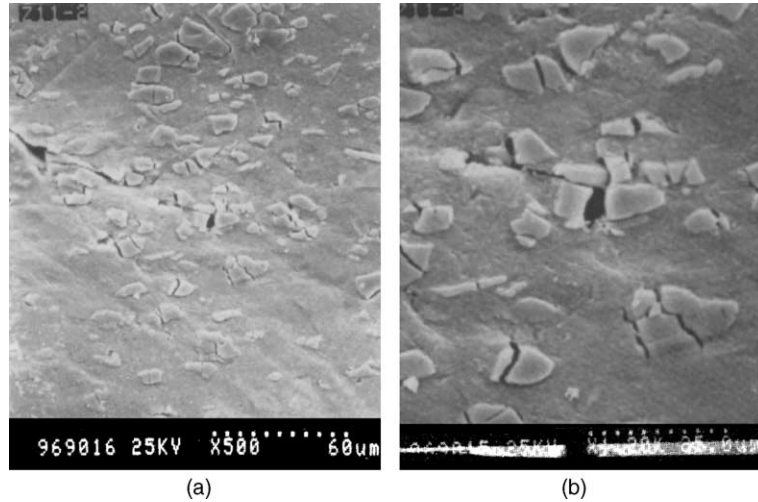


Fig. 5. Failure characteristics in the crack tip: (a) macro-crack showing the cracked SiC particles and (b) phenomenon of SiC particles broken and no-damage of matrix in the crack-tip region.

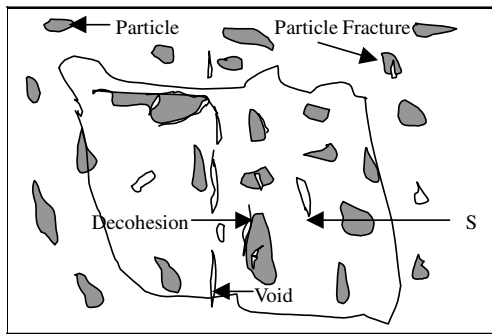


Fig. 6. Schematic of MMCs failure in three forms: Matrix failure as in the form of voids, particulate broken and particle/matrix interface de-cohesion.

ation and growth; particle breakage and particle/matrix interface de-cohesion. Fig. 6 shows a schematic of the MMCs failure. The presence of SiC reinforcement is typically detrimental to the fracture resistance of a composite due to the addition of reinforcement fracture, reinforcement/matrix interface decohesion and/or reinforcement fracture within the clusters compared to the failure mechanisms of un-reinforced aluminum alloy.

3.3. Damage and failure threshold

The damage threshold and complete failure threshold can be described by a plane of applied

mechanical load and laser beam energy density, i.e. a plane of $\sigma_{\max}-E_j$. The damage occurred in two forms, matrix failure in the form of voids and particle/matrix interface de-cohesion. By analyzing the SEM micrographs with a magnification of 500, the damage threshold was defined as the point at which one could observe voids in the matrix or between the matrix/particle interfaces. The complete failure threshold was defined as the point at which the single-notched sample was completely fractured. Fig. 7 shows the experimental results for the plane of $\sigma_{\max}-E_j$. The damage threshold and failure

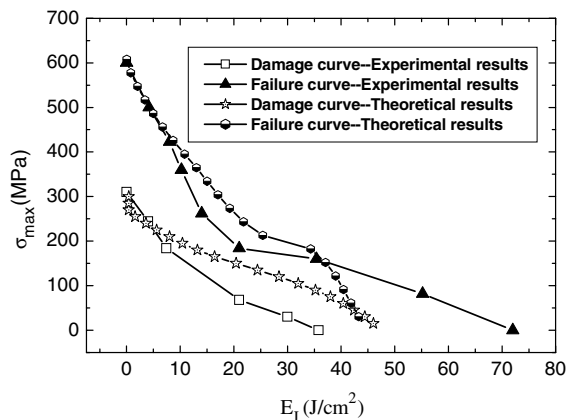


Fig. 7. Damage and failure threshold plane.

threshold for applied mechanical load with no laser beam heating are $\sigma_{\max}^{\text{Dth}} = 300$ MPa and $\sigma_{\max}^{\text{Fth}} = 600$ MPa, respectively. The damage threshold and failure threshold for laser beam heating load with no applied mechanical load are $E_J^{\text{Dth}} = 36$ J/cm² and $E_J^{\text{Fth}} = 72$ J/cm², respectively. According to the level of damage and failure, three regions, namely, a non-damaged region, a damaged region and a failure region, can be defined. The non-damage region is located on the down left of the damage curve. The damage region is between the damage curve and failure curve. The failure region is located on the upper right of the failure curve. One can see that the contribution of the applied mechanical load and laser beam thermal load to the damage and failure of MMCs is non-linear. In other words, their contributions are coupled. If the mechanical load is between the damage threshold $\sigma_{\max}^{\text{Dth}}$ and complete failure threshold $\sigma_{\max}^{\text{Fth}}$, an additional thermal load, with a little laser energy density, will lead to complete failure of the samples. This region is called a laser beam sensitive region. In the same way, when the laser energy density is high enough, an additional little mechanical load will also make the sample completely fail.

4. Discussions

4.1. Theoretical model

As described above, the mechanism of initial damage is the formation of voids in the matrix and separation at the SiC particle–matrix interface. However, the mechanism of crack propagation is dominated by SiC particle fracture. This section describes a theoretical model proposed to explain the interesting experimental phenomena and to predict the damage threshold and failure threshold. According to the model, the temperature rise and thermal stress are first obtained, then the maximum stresses in reinforced particles and at matrix/particle interfaces are determined, the stress intensity factors are finally obtained.

4.1.1. Thermal stress

Surface and internal temperature in the composite materials can be determined by the diffusion equation

$$\rho C_p \frac{\partial \vartheta}{\partial t} = k \left(\frac{\partial^2 \vartheta}{\partial r^2} + \frac{1}{r} \frac{\partial \vartheta}{\partial r} \right) + \frac{I(r, t)(1 - R_0)}{h} \quad (3)$$

where $I(r, t)$ is the intensity of the incident laser beam, r is the coordinate in the radial direction and the origin is taken as the center of the laser spot, t is time, $\vartheta(r, t)$ is the temperature rise and R_0 is the reflection coefficient which can be experimentally determined and is equal to 0.4 approximately. In the above formulas, k , ρ , C_p and h are the thermal conductivity, density, specific heat capacity of the materials and thickness of the sample, respectively. Generally, as described by Eqs. (1) and (3), the temperature rise should be a function of time and space. However, the finite element simulation, which will be discussed in later, shows that the temperature rise inside the laser-irradiated region is almost uniform even after 600 μ s, and after a time of 1.5 ms the temperature gradient in the thickness direction is also zero. This means that the heat conductivity in the radial direction is almost ignored. Therefore, the temperature rise within the laser-irradiated region is approximately

$$\vartheta = \begin{cases} \frac{E_J(1-R_0)}{\rho C_p h}, & 0 \leq r \leq a_0 \\ 0, & r \geq a_0 \end{cases} \quad (4)$$

where a_0 is the radius of the laser spot. The temperature within the laser-irradiated region is much high than that of the outer side of the laser spot. The high thermal expansion within the laser-irradiated region is constrained by the cooler edge. This causes tensile hoop stresses at the laser spot edge and tangential and radial compressive stresses in the laser spot region. For simplicity, the sample is assumed to be a disk and the thermal stresses are calculated under a plane stress condition. Only tangential thermal stress $\sigma_{\theta\theta}(r, t)$ has a contribution to crack forming and opening, and it is described as

$$\sigma_{\theta\theta} = -\frac{1}{2} \alpha E^c \frac{E_J(1.0 - R_0)}{\rho C_p h} \left[1 - \left(\frac{a_0}{R} \right)^2 \right], \quad 0 < r < a_0 \quad (5)$$

$$\sigma_{\theta\theta} = \frac{1}{2} \alpha E^c \frac{E_J(1.0 - R_0)}{\rho C_p h} \left[\left(\frac{a_0}{r} \right)^2 + \left(\frac{a_0}{R} \right)^2 \right], \quad a_0 < r < R \quad (6)$$

where α is the thermal expansion coefficient of composites, R the radius of the disk, E^c is the Young's modulus of composite. It is easily seen that tangential thermal stresses $\sigma_{\theta\theta}(r, t)$ remain as negative values within the laser spot region and positive values around the laser spot region, respectively.

4.1.2. Stress in particle and at matrix/particle interfaces

It is well known that the reinforcement of a hard ceramic particle in a soft metallic matrix produces composite with substantially higher yield strength than that of the matrix. Nardone and Prew (1986) and Nardone (1987) proposed a modified shear lag (MSL) model based on shear lag theory, ascribing the entire strengthening effect to the load-bearing feature of hard reinforcement. On the other hand, Arsenault et al. (1991) thought that the strengthening mainly attributed to the enhanced strength of the matrix because of the increase in dislocation density in matrix by a few orders of magnitude.

The idea of stress transfer between the matrix and hard particles is used to explain the failure mechanism. As a ductile metal matrix is stressed to certain extent, it typically undergoes plastic deformation, whereas, the reinforced particles generally deform still elastically due to the much higher Young's modulus. Several studies on the state of stress and strain at the interface between a rigid or elastic particle and a plastically deforming matrix have been performed, for both cylindrical and spherical particles (Eshelby, 1957a,b; Wilner, 1988). However, Lee and Mear (1999) predicted that for non-equiaxed particles, the stress concentration at the particle/matrix interface would be substantially different from that for equiaxed inclusions. Furthermore, the stress concentration within the particle would be very high such that particle fracture would precede interfacial debonding. We consider now the axisymmetric problem of an elastic reinforced particle (E^p, ν^p) embedded in an infinite elastic matrix (E^c, ν^c), where the superscripts p and c denote the reinforced particle and MMCs, respectively. The complete solution to this problem is given by Eshelby (1957a,b). He found that, the stress and

strain fields inside the reinforced particle were uniform. For tensile loads, the largest normal interfacial stress always occurs at the poles of the reinforced particle and is equal to

$$\sigma^p = \left[\frac{2(1-\kappa)}{3 \frac{G^c}{G^p}(1-B) + 3B} + \frac{1+2\kappa}{3 \frac{K^c}{K^p}(1-A) + 3A} \right] S \quad (7)$$

Here G^p and G^c are the shear moduli of the reinforced particle and of the matrix respectively, K^p and K^c are the bulk moduli, A and B are the Eshelby coefficients, which are given by

$$A = \frac{1+\nu^c}{3(1-\nu^c)}, \quad B = \frac{2(4-5\nu^c)}{15(1-\nu^c)} \quad (8)$$

S is the tensile load in the infinite place and $k = T/S$ is a triaxiality parameter that is considered in the range from zero to one. According to the results of Eshelby (1957a,b), the largest normal stress along the interface is equal to the largest normal stress in the particle, i.e., $\sigma_i = \sigma_p$. The largest shear stress along the interface is always at 45° to the tensile direction and equals

$$\tau_i = \frac{\frac{3}{2}(1-\kappa)}{3 \frac{G^c}{G^p}(1-B) + 3B} S \quad (9)$$

An empirical power law such as the Ramberg–Osgood relation can reasonably express the uniaxial stress–strain behavior for a kind of metal matrix materials

$$\varepsilon = \frac{\sigma^m}{E^m} + \frac{3}{7} \frac{\sigma_0^m}{E^m} \left(\frac{\sigma^m}{\sigma_0^m} \right)^{1/N} \quad (10)$$

where σ^m and ε are the axial stress and strain of matrix, respectively; σ_0^m is its yield strength; N is the hardening exponent. However, the matrix was reinforced by the hard ceramic particle. Many researchers have studied the stress–strain relation of particle-reinforced MMCs. In their investigations, the uniaxial response of MMCs is assumed to take the form of the following relation which was obtained by Brockenbrough and Zok (1995) with finite element calculations,

$$\frac{\sigma^c(\varepsilon)}{\sigma^m(\varepsilon)} = \bar{\rho}(\varepsilon)(1 - \gamma f - \xi f^2) + [1 - \bar{\rho}(\varepsilon)] \times [1 + \bar{\alpha} \tan(3\pi f/4) + \bar{\beta} f^3] \quad (11)$$

where $\sigma^c(\varepsilon)$ is the axial stress in MMCs, and other coefficients are given in the following,

$$\bar{\alpha}(N) = 0.15 + 0.913N,$$

$$\bar{\beta}(N) = 2.86 + 21.4N, \quad \gamma(N) = 0.916 - 1.61N$$

$$\xi(N) = 0.01 + 0.828N,$$

$$\bar{\rho}(\varepsilon) = 1 - e^{-[\delta(\sigma^m(\varepsilon)/(\sigma_0^m))]} \quad (12)$$

In the expressions, f is volume fraction of the reinforced particle, $\bar{\rho}(\varepsilon)$ represents the level of damage as a function of strain, δ represents the ratio of particle stress to the reference strength at a strain of $\varepsilon = \varepsilon^* = \sigma_0^m/E^m$. In order to determine the largest stress in the reinforced particle and along the interface, the secant Young's modulus of MMCs, defined by the ratio of tensile stress to the tensile strain (Nan and Clarke, 1996), is given by

$$E^c = \frac{E^m}{1 + \frac{3}{7} \left(\frac{\sigma_0^m}{\sigma_0^c} \right)^{\frac{1}{n}-1}} \left\{ \bar{\rho}(\varepsilon)(1 - \gamma f - \xi f^2) + [1 - \bar{\rho}(\varepsilon)][1 + \bar{\alpha} \tan(3\pi f/4) + \bar{\beta} f^3] \right\} \quad (13)$$

Other parameters such as shear modulus G^c , bulk modulus K^c and Poisson's ratio can also be obtained as,

$$G^c = \frac{E^c}{2(1 + \nu^c)} \quad K^c = \frac{E^c}{3(1 - 2\nu^c)} \quad (14)$$

In this case, the maximum stresses in a particle and at the matrix/particle interfaces can easily be determined by expressions (7) and (9). The theoretical model can be used to study the failure mechanism and damage threshold in MMCs induced by the coupled effect of laser beam heating and mechanical load.

4.1.3. Stress intensity factors

Once the micro-cracks have formed, they may propagate due to the increase of laser beam energy density or applied mechanical load. In this

section, a model for predicting the complete failure is proposed. The weight function method is used to calculate the thermal stress intensity factor K_I^T of the single edge notched sample induced by laser beam thermal load. Starting with the known solution of constant stress σ_0 on the crack faces, the stress intensity factor of an arbitrary thermal stress distribution $\sigma_{\theta\theta}$ induced by laser heating has the following solution according to Wu (1984)

$$K_I^T = \Phi \sigma_0 \sqrt{\pi c} \quad (15)$$

$$\Phi = \frac{1}{\varsigma \sqrt{2\pi\beta_0(\varsigma)}} \int_0^\varsigma \frac{\sigma_{\theta\theta}(x)}{\sigma_0} \times [\beta_1(\varsigma)(\varsigma - x)^{-1/2} + \beta_2(\varsigma)(\varsigma - x)^{1/2} + \beta_3(\varsigma)(\varsigma - x)^{3/2}] dx \quad (16)$$

where c is the crack length, w is the width of the sample and $\varsigma = c/w$. The coefficients $\beta_1(\varsigma)$, $\beta_2(\varsigma)$ and $\beta_3(\varsigma)$ are given in the Appendix A. Integrating Eq. (Wilner, 1988), we can easily obtain the thermal stress intensity factor K_I^T just by simply substituting

$$\sigma_0 = \frac{1}{2} \alpha E^c \frac{E_J(1 - R_0)}{\rho C_p h} \quad (17)$$

and

$$\Phi = \frac{1}{\sqrt{2\pi\beta_0(\varsigma)}} \frac{1}{\varsigma} H(\varsigma) \quad (18)$$

into Eq. (15), where

$$H(\varsigma) = \begin{cases} H_1(\varsigma) & 0 \leq \varsigma \leq r_0^* - a_0^* \\ H_1(r_0^* - a_0^*) - E^*(T)(1 - \eta^2)H_2(\varsigma) & r_0^* - a_0^* \leq \varsigma \leq r_0^* + a_0^* \\ H_1(r_0^* - a_0^*) - E^*(T)(1 - \eta^2)H_2(r_0^* + a_0^*) + H_3(\varsigma) & r_0^* + a_0^* \leq \varsigma \leq 1 \end{cases} \quad (19)$$

and $r_0^* = r_0/w$, $a_0^* = a_0/w$ and $H_1(\varsigma)$, $H_2(\varsigma)$, $H_3(\varsigma)$ are given in the Appendix A.

The stress intensity factor, induced by the applied mechanical loading $\sigma = \sigma_{\max}/\alpha_\sigma$, has the following expression (Tada et al., 1973),

$$K_I^m = F_1(\varsigma) \sigma \sqrt{\pi c} \quad (20)$$

where

$$F_I(\varsigma) = \sqrt{\frac{2}{\pi\varsigma} \tan\left(\frac{1}{2}\pi\varsigma\right)} \times \frac{0.752 + 2.02\varsigma + 0.37[1 - \sin(\frac{1}{2}\pi\varsigma)]^3}{\cos(\frac{1}{2}\pi\varsigma)} \quad (21)$$

Consequently, the stress intensity factor K_I , for the specimen subjected to the coupled loads (σ_{\max}, E_J) , should be written as,

$$K_I = K_I^T + K_I^m \quad (22)$$

Therefore, the stress intensity factors for the specimen subjected to the coupled loads (σ_{\max}, E_J) can be used to predict the complete failure threshold and the results are discussed in the following section. Here, the contribution of laser heating to the crack propagating will be discussed. As discussed above, the thermal stress $\sigma_{\theta\theta}$ induced by laser heating is always compressive within the laser spot region and is tensile around the laser spot region. The compressive thermal stress within laser-irradiated region will be responsible for the close of the crack contrary to the compressive thermal stress, the tensile stress around the laser spot region will be responsible for the crack opening (Zhou et al., 2001a). Therefore, the thermal stress, induced by laser heating, would have a contribution to the stress intensity factor, as described by Eq. (15). On the other hand, the laser heating will induce the temperature rise within laser-irradiated region and, hence, the material's fracture toughness will decrease.

4.2. Finite element simulation and temperature fields

In order to check the validity of the theoretical model, the finite element simulations are carried out for the temperature field induced by laser heating, stress fields induced by the combined laser heating and applied mechanical tensile load. Furthermore, the maximum stresses in the particle and matrix are also simulated by considering the plasticity of the matrix for different couple loads (σ_{\max}, E_J) .

The ANSYS/LS-DYNA program is used to simulate the above problem. For the temperature field simulation, the material is assumed to be homogenous and the material parameters of MMCs are listed in Table 2. The temperature fields are governed by the following heat conductivity equation,

$$\rho C_p \frac{\partial \vartheta}{\partial t} = k \left(\frac{\partial^2 \vartheta}{\partial^2 r} + \frac{1}{r} \frac{\partial \vartheta}{\partial r} + \frac{\partial^2 \vartheta}{\partial^2 z} \right) \quad (23)$$

here z denotes the coordinate in the thickness direction. The heat is assumed to be the absorption of the laser energy, i.e., $k \partial \vartheta / \partial z|_{z=0} = -(1 - R_0)I(r, t)$. The temporal shape and spatial distribution of the laser beam are described by expressions (1) and (2). In the simulation, the boundary condition is assumed to be adiabatic, i.e. there is neither and that there is not any other heat source, nor any other heat loss on the front and back surface of the specimen. A representative mesh with 7630 elements and 2510 nodes for the temperature rise calculation is shown in Fig. 8.

In order to study the stress in the particle and at the interface of MMCs, a two-dimensional unit cell model is used to represent the whole composite

Table 2
Material properties

| Parameters | Al Matrix | SiC Particle | MMCs |
|--|-----------|--------------|-------|
| Young's modulus (GPa) | 68.3 | 427 | 122 |
| Yield strength (MPa) | 97.0 | — | — |
| Poisson's ratio | 0.33 | 0.17 | 0.30 |
| Thermal expansion coefficients ($10^{-6} \text{ }^\circ\text{C}^{-1}$) | 23.6 | 4.8 | 20.78 |
| Thermal conductivity coefficients (W/cm K) | 1.8 | 0.42 | 1.206 |
| Density (g/cm^3) | 2.7 | 3.21 | 2.82 |
| Specific heat capacity (J/g K) | 0.84 | 2.54 | 1.845 |
| Tensile strength (MPa) | 278 | 950 | 600 |
| Percentage elongation (%) | 14.5 | 0.8 | 6 |

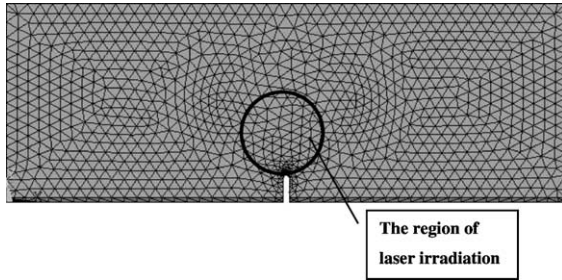


Fig. 8. A representative mesh for the calculation model of temperature rise.

and the representative mesh of the unit cell with 742 elements and 780 nodes is shown in Fig. 9. In the unit cell, the reinforced particle is assumed to be a SiC particle with a radius of 10 μm . The matrix is assumed as the MMCs and its stress–strain relationship is described by Eq. (11). The material constants are also listed in Table 2. In the simulation, the boundary condition is shown in Fig. 9 with the tensile stress S in the x -direction and the free boundary condition in the y -direction. For a pair of coupled loads (σ_{\max}, E_J) , the stress field can be simulated. The stress concerned is the maximum stress in the particle and interface.

Here, the characteristics of the temperature fields are given, and the spatial and temporal distributions of temperature fields are shown in Fig. 10(a) and (b) respectively. Fig. 10(a) shows the temperature fields on the front surface, i.e. the laser-irradiated surface for a time of 600 μs with laser energy density of 40 J/cm^2 . It is shown that

the spatial distribution of temperature even for a time of 600 μs is almost the same as the spatial distribution of laser intensity. The temperature is almost uniform within the laser-irradiated region and declines very sharply toward the edge where the laser spot terminates. Fig. 10(b) shows the histories of the temperature, both on the front and on the rear surfaces around the center of the laser-irradiated region. It is shown that the temperature gradient in the thickness direction is almost zero after 1.5 ms. From Fig. 10, it can be concluded that the temperature gradient is almost zero after 1.5 ms and the temperature conductivity in the r -direction is almost zero even at a time of 600 μs . Therefore, the assumption of Eq. (4) is suitable.

4.3. Damage initiation

The laser beam heating will make the yield strength Y_0 and tensile strengths σ_1^* of the matrix degrade at an elevated temperature ϑ . According to the test results of tensile strength for Al alloy at different temperatures (Wang and Huang, 1996), the fitting equations of σ_1^* as a function of temperature is obtained by an approximation of polynomial function

$$\sigma_1^* = 280F(T) \text{ (MPa)} \quad (24)$$

where

$$F(T) = 1.0 - 6.41 \times 10^{-3}\vartheta + 6.0 \times 10^{-5}\vartheta^2 - 2.20 \times 10^{-7}\vartheta^3 \quad (25)$$

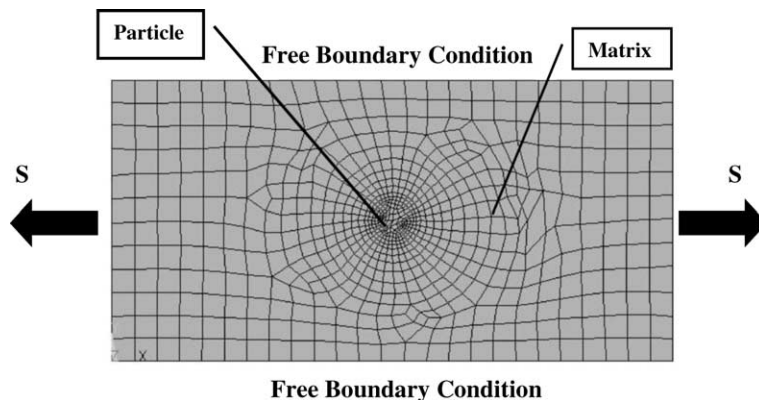


Fig. 9. A representative mesh for the calculation model of stress fields near the reinforced particle.

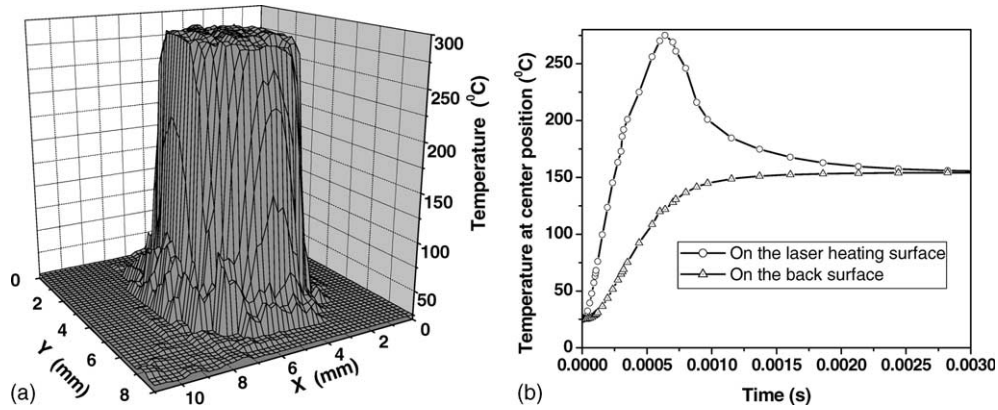


Fig. 10. Temperature fields: (a) two-dimensional distribution of temperature on the laser irradiated surface induced by laser heating with laser energy density of 40 J/cm^2 at time of $600 \mu\text{s}$ and (b) temperature histories at the center of laser irradiated region both on the front and rear surface of specimen with laser energy density of 40 J/cm^2 .

It is assumed that the degradation of reinforcement is negligible. As we know from the above experimental observations, the interfacial debonding and matrix damage were the main damage mechanism. It is difficult to measure the interface fracture toughness of SiC/Al in the MMCs. However, the experimental results of Shaw et al. (1993) show that the interface fracture toughness of $\text{Al}/\text{Al}_2\text{O}_3$ or $\text{Cu}/\text{Al}_2\text{O}_3$ with two layers should be helpful in evaluating the interface fracture toughness of SiC/Al in the MMCs. The results given by Shaw et al. (1993) show that the interface fracture toughness of $\text{Al}/\text{Al}_2\text{O}_3$ or $\text{Cu}/\text{Al}_2\text{O}_3$ would increase as the increase of metal thickness. When the metal thickness is very small, for example, $50 \mu\text{m}$, the interface fracture toughness of $\text{Al}/\text{Al}_2\text{O}_3$ or $\text{Cu}/\text{Al}_2\text{O}_3$ would be close to the fracture toughness of the ceramic. Based on this result, it was assumed reasonably that the interface fracture toughness of SiC/Al in the MMCs is just the fracture toughness of the SiC reinforced particle, due to the fact that the average space distance of particles is about $15 \mu\text{m}$. On the other hand, the degradation of the matrix at elevated temperature will reduce the interface fracture toughness of SiC/Al in the MMCs. Eventually, it was assumed that the interface fracture toughness of the SiC/Al in the MMCs is,

$$K_c = K_{\text{SiC}} F(T) \quad (26)$$

where $K_{\text{SiC}} = 3 \text{ MPa}\sqrt{\text{m}}$ is the fracture toughness of the SiC reinforced particle (Cai and Bao, 1998). The mechanical stress at the notch-tip was $\sigma_{\text{max}} = \alpha_\sigma \sigma$. Let $S = \sigma_{\theta\theta}(r, t) + \sigma_{\text{max}}$ in Eqs. (7) and (9), for a pair of $(E_J, \sigma_{\text{max}})$, we can easily obtain the largest stress σ^p in the particle and the largest interfacial shear stress τ_i . For convenience of analysis, the material parameters are listed in Table 2. The parameters of the stress-strain relation of the matrix are taken from the paper of Brockenbrough and Zok (1995) with $N = 0.2$, $\delta = 0.1$. It should be pointed out that the combined mechanical and thermal load for damage initiation is only valid at the root of the notch, since the assumed stress concentration due to mechanical load is at the root. Thus, only particles and interfaces that are situated at the root are eligible for such a quantification. It is well known that the interface crack is a mixed mode crack (Rice, 1988). The stress intensity factor of the SiC/Al interface crack in MMCs could be written as

$$K_{\text{in}} = \sqrt{K_{\text{inI}}^2 + K_{\text{inII}}^2} = \sqrt{2\pi d(\sigma_i^2 + \tau_i^2)} \quad (27)$$

where K_{inI} and K_{inII} are the mode I and mode II stress intensity factors of the SiC/Al interface crack in MMCs respectively and d is the average size of the reinforced particle.

Fig. 11(a) and (b) show the largest interfacial normal stress σ_i of theoretical model and simulation results, respectively, as a function of E_J for

different σ_{\max} . Fig. 12(a) and (b) show the largest interfacial shear stress τ_i for the theoretical model and simulation results, respectively, as function of E_j for different σ_{\max} . Fig. 13(a) and (b) show the interface stress intensity factors of the SiC/Al in MMCs for the theoretical model and simulation results, respectively, as function of E_j for different σ_{\max} . The interfacial strength K_c , as a function of laser energy density, is also indicated in the figure. Fig. 14(a) and (b) show the largest stress in the reinforced particle for the theoretical model and simulation results, respectively, as well as the

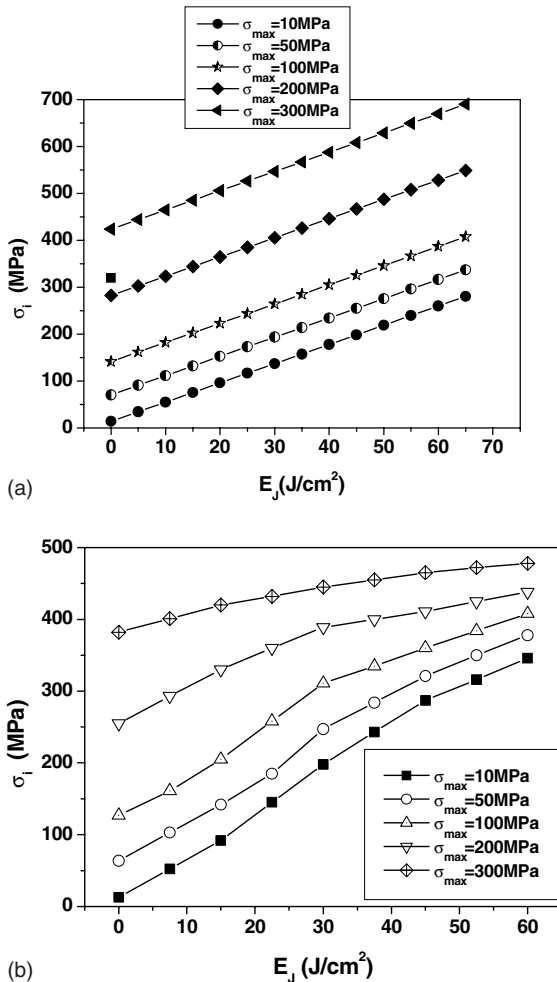


Fig. 11. The largest interfacial normal stress σ_i as a function of E_j for different σ_{\max} : (a) theoretical model results and (b) FEM simulation results.

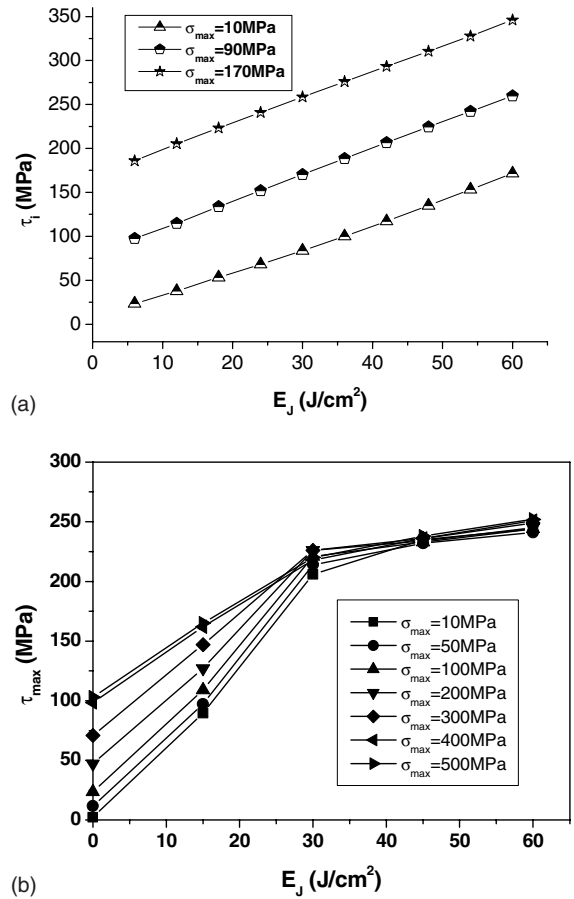
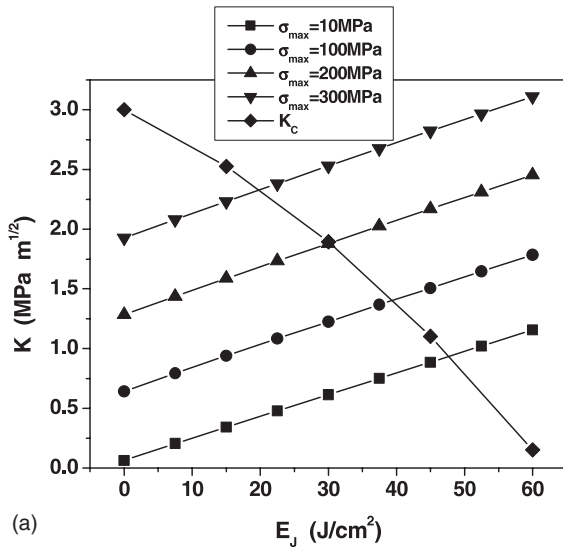
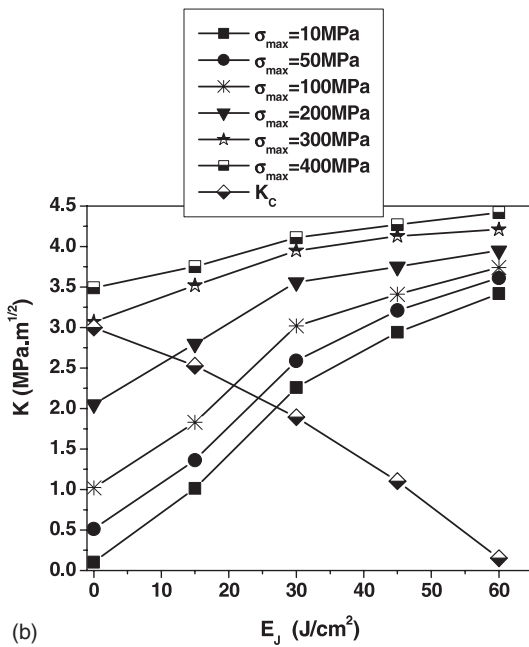


Fig. 12. The largest interfacial shear stress τ_i as a function of E_j for different σ_{\max} : (a) theoretical model results and (b) FEM simulation results.

particle strength σ_c^p , the estimation of which follows. It is seen that the normal stress increases when laser energy density and applied mechanical load increase. However, the interfacial strength decreases due to the high temperature degradation when laser energy density increases. It is easily seen that interface stress intensity factors may be larger than the interface strength. However, the largest stress σ^p in the particle is much lower than the strength of the SiC particle. The results can explain why the mechanism of void formation in the matrix and separation of the reinforcement/matrix was produced in the micro-crack initiation, and why the reinforcement particles did not fracture in the period of initial crack formation. When



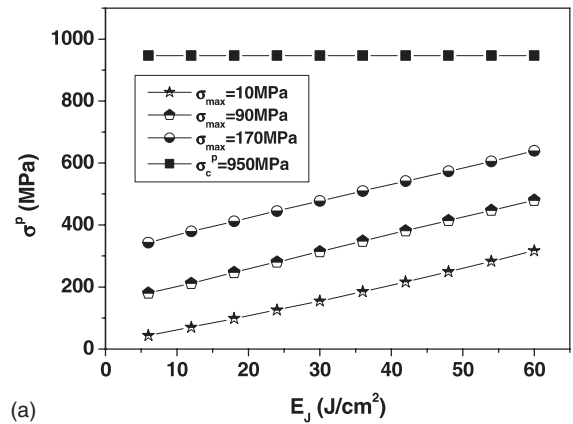
(a)



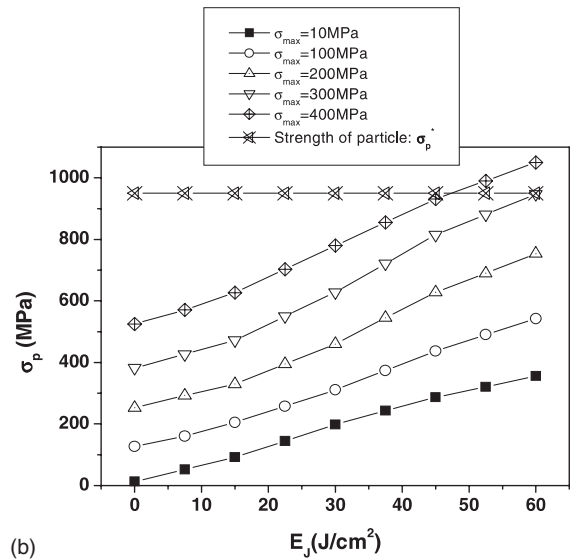
(b)

Fig. 13. The interface stress intensity factors of SiC/Al in MMCs as a function of E_J for different σ_{\max} : (a) theoretical model results and (b) FEM simulation results. Here, the interfacial strength K_c as a function of laser energy density is also indicated in the figure.

the MMCs were subjected to laser beam heating, the strength of the matrix was degraded at elevated temperature, i.e. the yield strength decreased. In



(a)



(b)

Fig. 14. The largest stress in a reinforced particle as a function of E_J for different σ_{\max} : (a) theoretical model results and (b) FEM simulation results.

this case, the particle loading through the interface was so low that SiC particle cracking did not take place. But the localized thermal stresses, due to the rapid changes in temperature, sometimes lead to the nucleation of micro-cracks within matrix/reinforcing interface or in matrix. More commonly, however, these thermal stresses lead to the growth of pre-existing cracks. If the applied stress is large enough, these micro-cracks may grow into macroscopic cracks and lead to the propagation of the macro-crack. However, there are some

differences between the theoretical model and the simulation results. The stress resulting from the theoretical model is linear, but non-linear for the simulation results. For high coupled load (σ_{\max}, E_J), the maximum stresses at the interface and in the particle are higher for the theoretical model results than that for the simulation results. For low coupled load (σ_{\max}, E_J), the maximum stresses at the interface and in the particle are almost at the same level for both the theoretical model and the simulation results.

4.4. Crack propagation

After micro-cracks formed in the notched region they would grow into a macro-crack. The mechanism of crack propagation is discussed in this section. The particle is considered to be broken if the stress in the particle exceeds the Griffith criterion

$$\sigma_c^p = K_c^p / \sqrt{d} \quad (28)$$

where K_c^p is a constant related to the fracture toughness of the particle together with geometrical factors (Nan and Clarke, 1996), and d is particle size. In MMCs, the value of constant K_c^p is also related to the metal matrix. A particle in the MMCs having higher strength than that of metal matrix generally has a higher fracture stress σ_c^p (Kiser et al., 1996). The value of parameter K_c^p , in Eq. (28), is preferred to be $K_c^p = 3.0 \text{ MPa}\sqrt{m}$ for SiC particles (Cai and Bao, 1998). Therefore, the fracture stress of SiC, with average size 10 μm , is 950 MPa.

As we know, the strain rate at the crack tip is very high, and even as high as $\approx 2.0\text{--}3.0 \times 10^3 \text{ s}^{-1}$ (Zhou et al., 1997). As a result of the high strain rates or the matrix hardening, the matrix yield stress increases significantly. The yield stress of the matrix is estimated as 390 MPa for a strain rate of $2.0 \sim 3.0 \times 10^3 \text{ s}^{-1}$ (Wang et al., 1988). Fig. 15(a) and (b) show the average stresses σ^c/σ_0^m in MMCs, i.e. the stress in a particle σ^p/σ_0^m or σ^p/σ_c^p as a function of remote strain $\varepsilon/\varepsilon_0^m$, and simulation results, respectively, where $\sigma_0^m = 390 \text{ MPa}$ and ε_0^m are the yield stress and yield strain of the matrix, respectively. In the case of matrix hardening, the

stresses in a particle may be so high that the particle will fracture. For example, for the remote strain $\varepsilon/\varepsilon_0^m = 4$, we have $\sigma^p/\sigma_0^m = 3.0$ and, equivalently, the stress in a particle will be 1170 MPa. It is clearly seen that the stress in a particle is higher than the fracture strength 950 MPa. However, the stress in the matrix is the yield stress and it is lower than the matrix strength. Therefore, one may conclude that the particle is broken and the matrix is not damaged, which is consistent with the experimental phenomenon as mentioned above. The simulation results also show that the maximum

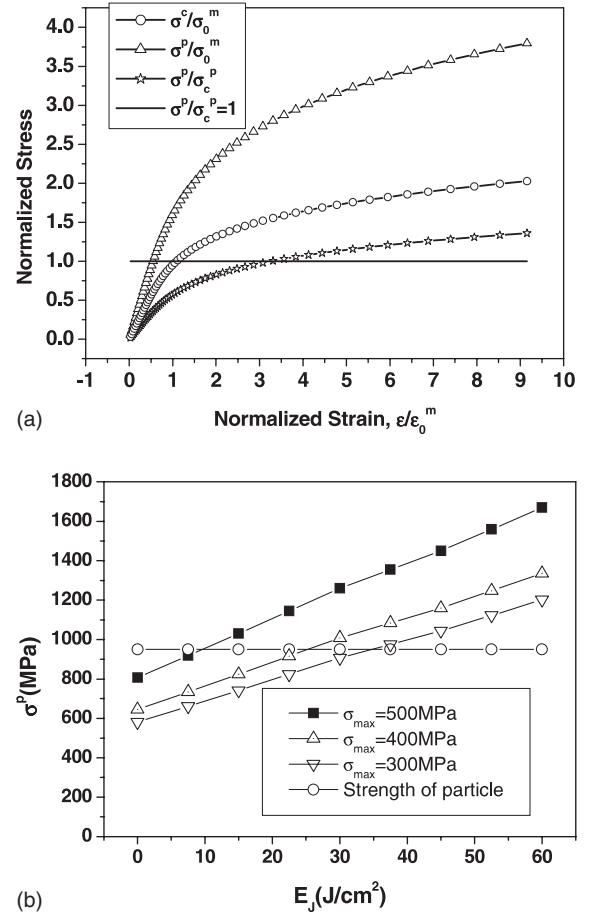


Fig. 15. The largest normal stress in particle: (a) the theoretical model results of average stresses in MMCs σ^c/σ_0^m stress in particle σ^p/σ_0^m or σ^p/σ_c^p as a function of remote strain $\varepsilon/\varepsilon_0^m$ where $\sigma_0^m = 390 \text{ MPa}$ and ε_0^m are the yield stress and yield strain of matrix, respectively; and (b) FEM simulation results.

stress in the particle is higher than the strength of the particle.

4.5. Damage and failure thresholds

The damage threshold is determined by the criterion that the interface stress intensity factor is higher than the interface strength. For a pair parameter of (σ_{\max}, E_J) , we can obtain the largest shear stress τ_i along the interface and largest interfacial normal stress σ_i for theoretical model. After that, the interface stress intensity factor could be easily obtained from Eq. (27). In this case, the damage threshold can easily be determined and the results are shown in Fig. 7.

For a pair parameter of (σ_{\max}, E_J) , we can obtain the stress intensity factor K_I or energy release rate $G_I = K_I^2/E^c$. When the following condition is satisfied the crack will propagate an increment Δc ,

$$K_I \geq K_{IC} \quad \text{or} \quad G_I \geq G_{IC} \quad \text{and} \quad \frac{\partial G_I}{\partial c} \geq \frac{\partial G_{IC}}{\partial c} \quad (29)$$

where the fracture toughness K_{IC} and crack-growth resistance G_{IC} of MMCs, at elevated temperature, are taken from the experimental results (Somerday et al., 1995). In this case, the failure threshold can be determined and the results are shown in Fig. 7.

One can see that the theoretical results, for both the damage threshold and failure threshold, well match the experimental results in the case of the low laser energy density E_J . When the laser energy is medium, the theoretical results for both damage threshold and failure threshold are higher than that found in the experimental results. However, high laser energy density E_J results in a large difference between the theoretical and experimental results. The low laser energy density means that the coupled degree of applied mechanical load with laser thermal shock load is low. Therefore, the theoretical model is applicable in the prediction of the damage and failure threshold for a low laser energy density. Consequently, the theoretical model is suitable to predict the damage and failure threshold for a lowly coupled degree of applied mechanical load with laser thermal shock load. Nevertheless, the proposed theoretical model is

invalid for predicting the damage and failure threshold for a highly coupled degree of far-field mechanical load with laser thermal shock load. This may be due to the neglect of visco-plastic deformation for MMCs at high temperature. One can see the non-linear coupled effect of far-field mechanical load with laser beam thermal load on the MMC failure from the plane of $\sigma_{\max}-E_J$.

5. Conclusions

The failure of particle-reinforced MMCs, induced by laser beam thermal shock and mechanical load, is experimentally and theoretically studied. It is found that the initial crack occurs in the notched-tip region and is induced by void nucleation, growth and subsequent coalescence in the matrix materials or separation of the interface. However, the process of crack propagation is caused by fracture of the SiC particulate, which is much different from the crack initiation mechanism. The damage threshold and complete failure threshold could be described with a plane of applied mechanical load σ_{\max} with laser beam energy density E_J . A theoretical model was proposed to explain the damage/failure mechanism and to calculate the damage threshold and complete failure threshold. The model is based on the idea of stress transfer, between the reinforced-particle and the matrix, and the calculation of an applied mechanical stress intensity factor and local thermal stress intensity factor. In order to check the validity of the theoretical model, the finite element simulations are presented for the temperature field, induced by laser heating, and stress fields, induced by the combined laser heating and applied mechanical tensile load. Both theoretical model and finite element simulation can explain the experimental phenomenon well. The failure of MMCs induced by laser thermal shock and applied mechanical load is non-linear. The theoretical model is also applicable in the prediction of the damage and failure threshold for a lowly coupled degree of applied mechanical load with laser thermal shock load. However, the problem of defining a coupled coefficient, which is used to describe the coupled degree of applied mechanical load with laser

thermal shock load, as well as the problem of finding a suitable theoretical model to predict the damage and failure threshold, for a highly coupled degree of applied mechanical load with laser heating, need further investigation.

Acknowledgements

Support for this research program was provided partly by the NNSF of China (No. 19772043) and the great research item (KJ951-1-201) of Chinese Academy of Sciences. The authors would like to thank Dr. Qunjia Peng for helpful discussion.

Appendix A

In this appendix, some coefficients are given as

$$\beta_0(\varsigma) = \alpha_0 + \alpha_1\varsigma + \alpha_2\varsigma^2 + \alpha_3\varsigma^3 + \alpha_4\varsigma^4 \quad (\text{A.1})$$

with $\alpha_0 = 1.12$, $\alpha_1 = -0.23$, $\alpha_2 = 10.6$, $\alpha_3 = -21.7$, $\alpha_4 = 30.4$

$$\beta_1(\varsigma) = 2\beta_0(\varsigma)\varsigma^{1/2} \quad (\text{A.2})$$

$$\begin{aligned} \beta_2(\varsigma) = & 2\beta_0(\varsigma)\varsigma^{-1/2} + 4\frac{d\beta_0(\varsigma)}{d\varsigma}\varsigma^{1/2} \\ & + \frac{3}{2}\left[\frac{5\pi}{\sqrt{2}}\phi(\varsigma) - \frac{20}{3}\beta_0(\varsigma)\right]\varsigma^{-1/2} \end{aligned} \quad (\text{A.3})$$

$$\begin{aligned} \beta_3(\varsigma) = & -\frac{1}{2}\left[\frac{5\pi}{\sqrt{2}}\phi(\varsigma) - \frac{20}{3}\beta_0(\varsigma)\right]\varsigma^{-3/2} \\ & + \left[\frac{5\pi}{\sqrt{2}}\frac{d\phi(\varsigma)}{d\varsigma} - \frac{20}{3}\frac{d\beta_0(\varsigma)}{d\varsigma}\right]\varsigma^{-1/2} \end{aligned} \quad (\text{A.4})$$

$$\begin{aligned} \phi(\varsigma) = & \frac{1}{2}\alpha_0^2 + \frac{2}{3}\alpha_0\alpha_1\varsigma + \frac{1}{4}(\alpha_1^2 + 2\alpha_0\alpha_2)\varsigma^2 \\ & + \frac{2}{5}(\alpha_1\alpha_2 + \alpha_0\alpha_3)\varsigma^3 \\ & + \frac{1}{6}(2\alpha_0\alpha_4 + 2\alpha_1\alpha_3 + \alpha_2^2)\varsigma^4 \\ & + \frac{2}{7}(\alpha_1\alpha_4 + \alpha_2\alpha_3)\varsigma^5 + \frac{1}{8}(2\alpha_2\alpha_4 + \alpha_3^2)\varsigma^6 \\ & + \frac{2}{9}\alpha_3\alpha_4\varsigma^7 + \frac{1}{10}\alpha_4^2\varsigma^8 \end{aligned} \quad (\text{A.5})$$

$$\begin{aligned} H_1(\varsigma) = & \beta_1(\varsigma)[G_1(x_1 = 0, x_2 = \varsigma) \\ & + \eta^2 G(x_1 = 0, x_2 = \varsigma, n = -1)] \\ & + \beta_2(\varsigma)[G_2(x_1 = 0, x_2 = \varsigma) \\ & + \eta^2 G(x_1 = 0, x_2 = \varsigma, n = 1)] \\ & + \beta_3(\varsigma)[G_3(x_1 = 0, x_2 = \varsigma) \\ & + \eta^2 G(x_1 = 0, x_2 = \varsigma, n = 3)] \end{aligned} \quad (\text{A.6})$$

$$\begin{aligned} H_2(\varsigma) = & \beta_1(\varsigma)G(x_1 = r_0^*, x_2 = \varsigma, n = -1) \\ & + \beta_2(\varsigma)G(x_1 = r_0^*, x_2 = \varsigma, n = 1) \\ & + \beta_3(\varsigma)G(x_1 = r_0^*, x_2 = \varsigma, n = 3) \end{aligned} \quad (\text{A.7})$$

$$\begin{aligned} H_3(\varsigma) = & \beta_1(\varsigma)[G_4(x_1 = r_0^* + a_0^*, x_2 = \varsigma) \\ & + \eta^2 G(x_1 = r_0^* + a_0^*, x_2 = \varsigma, n = -1)] \\ & + \beta_2(\varsigma)[G_5(x_1 = r_0^* + a_0^*, x_2 = \varsigma) \\ & + \eta^2 G(x_1 = r_0^* + a_0^*, x_2 = \varsigma, n = 1)] \\ & + \beta_3(\varsigma)[G_6(x_1 = r_0^* + a_0^*, x_2 = \varsigma) \\ & + \eta^2 G(x_1 = r_0^* + a_0^*, x_2 = \varsigma, n = 3)] \end{aligned} \quad (\text{A.8})$$

$$\begin{aligned} G_1(x_1, x_2) = & \frac{a_0^*}{A}\left[\frac{\sqrt{A+By_2}}{y_2} - \frac{\sqrt{A+By_1}}{y_1}\right] \\ & + \frac{1}{2}\frac{B}{A}I(A, B, y_1, y_2) \end{aligned} \quad (\text{A.9})$$

$$\begin{aligned} G_2(x_1, x_2) = & a_0^*\left[\frac{\sqrt{A+By_2}}{y_2} - \frac{\sqrt{A+By_1}}{y_1}\right] \\ & - \frac{1}{2}Ba_0^*I(A, B, y_1, y_2) \end{aligned} \quad (\text{A.10})$$

$$\begin{aligned} G_3(x_1, x_2) = & a_0^*\left[\frac{(A+By_2)^{3/2}}{y_2} - \frac{(A+By_1)^{3/2}}{y_1}\right] \\ & - \frac{3}{2}a_0^*[2(A+By_2)^{1/2} - 2(A+By_1)^{1/2} \\ & + AI(A, B, y_1, y_2)] \end{aligned} \quad (\text{A.11})$$

$$\begin{aligned} G_4(x_1, x_2) = & -\frac{a_0^*}{A_1}\left[\frac{\sqrt{A_1+B_1z_2}}{z_2} - \frac{\sqrt{A_1+B_1z_1}}{z_1}\right] \\ & - \frac{1}{2}\frac{B_1}{A_1}J(A_1, B_1, z_1, z_2) \end{aligned} \quad (\text{A.12})$$

$$G_5(x_1, x_2) = -a_0^* \left[\frac{\sqrt{A_1 + B_1 z_2}}{z_2} - \frac{\sqrt{A_1 + B_1 z_2}}{z_2} \right] + \frac{1}{2} a_0^* B_1 J(A_1, B_1, z_1, z_2) \quad (\text{A.13})$$

$$G_6(x_1, x_2) = -a_0^* \left[\frac{(A_1 + B_1 z_2)^{3/2}}{z_2} - \frac{(A_1 + B_1 z_1)^{3/2}}{z_1} \right] + \frac{3}{2} a_0^* \left[2\sqrt{A_1 + B_1 z_2} - 2\sqrt{A_1 + B_1 z_1} \right] + A_1 J(A_1, B_1, z_1, z_2) \quad (\text{A.14})$$

$$G(x_1, x_2, n) = \frac{2}{2+n} [(\zeta - x_1)^{n/2+1} - (\zeta - x_2)^{n/2+1}] \quad (\text{A.15})$$

$$I(A, B, y_1, y_2) = \frac{2}{\sqrt{-A}} \left[\arctg \frac{\sqrt{A + B y_2}}{\sqrt{-A}} - \arctg \frac{\sqrt{A + B y_1}}{\sqrt{-A}} \right] \quad (\text{A.16})$$

$$J(A_1, B_1, z_1, z_2) = \frac{2}{\sqrt{A_1}} \left[\ln \frac{\sqrt{A_1 + B_1 z_2} - \sqrt{A_1}}{\sqrt{A_1 + B_1 z_2} + \sqrt{A_1}} - \ln \frac{\sqrt{A_1 + B_1 z_1} - \sqrt{A_1}}{\sqrt{A_1 + B_1 z_1} + \sqrt{A_1}} \right] \quad (\text{A.17})$$

$$A = \zeta - r_0^* \quad B = a_0^* \quad y_1 = \frac{r_0^* - x_1}{a_0^*} \quad y_2 = \frac{r_0^* - x_2}{a_0^*} \quad (\text{A.18})$$

$$A_1 = \zeta - r_0^* \quad B_1 = -a_0^* \quad z_1 = \frac{x_1 - r_0^*}{a_0^*} \quad z_2 = \frac{x_2 - r_0^*}{a_0^*} \quad (\text{A.19})$$

References

- Arsenault, R.J., Wang, L., Feng, C.R., 1991. Strengthening of composites due to microstructural changes in the matrix. *Acta Metall. Mater.* 39, 47–57.
- Berlin, P., Dickman, O., Larsson, F., 1992. Effects of heat radiation on carbon/PEEK, carbon/epoxy and glass/epoxy composites. *Composites* 23, 235–243.
- Brockenbrough, J.R., Zok, F.W., 1995. On the role of particle cracking in flow and fracture of metal matrix composites. *Acta Metall. Mater.* 43, 11–20.
- Cai, H., Bao, G., 1998. Crack bridging in functionally graded coatings. *Int. J. Solids Struct.* 35 (7–8), 701–717.
- Davidson, D.L., 1991. The effect of paniculate SiC on fatigue crack growth in a cast-extruded aluminum alloy composite. *Metall. Trans. A* 22, 97–123.
- Eshelby, J.D., 1957a. The determination of the elastic field of an ellipsoidal inclusion and related problems. *Proc. R. Soc. A* 241, 376–396.
- Eshelby, J.D., 1957b. The elastic field outside an ellipsoidal inclusion. *Proc. R. Soc.* 252, 561–569.
- Kiser, M.T., Zok, F.W., Wilkinson, D.S., 1996. Plastic flow and fracture of a particulate metal matrix composite. *Acta Mater.* 44 (9), 3465–3476.
- Lee, B.J., Mear, B.J., 1999. Stress concentration induced by an elastic spheroidal particle in a plastically deforming solid. *J. Mech. Phys. Solids* 47, 1301–1366.
- Li, C.S., Ellyin, F., 1999. A mesomechanical approach to inhomogeneous particulate composites undergoing localized damage. Part I: A mesodomain simulation. *Int. J. Solids Struct.* 36, 5529–5544.
- Llorca, J., 2002. Fatigue of particle- and whisker-reinforced metal matrix composites. *Prog. Mater. Sci.* 47 (3), 283–353.
- Nardone, V.C., Prewo, K.M., 1986. On the strength of discontinuous silicon carbide reinforced aluminum composites. *Scripta Metall.* 20, 43–48.
- Nardone, V.C., 1987. Assessment of models used to predict the strength of discontinuous silicon carbide reinforced aluminum alloys. *Scripta Metall.* 21, 1313.
- Nan, C.W., Clarke, D.R., 1996. The influence of particle size and particle fracture on elastic/plastic deformation of metal matrix composite. *Acta Mater.* 44 (9), 3801–3811.
- Podlesak, H., Schnick, T., Pawlowski, L., Steinhäuser, S., Wielage, B., 2000. Microscopic study of AlSiC particulate composites processed by laser shocks. *Surf. Coat. Technol.* 124, 32–38.
- Rabiei, A., Enoki, M., Kishi, T., 2000. A study on fracture behavior of particle reinforced metal matrix composites by using acoustic emission source characterization. *Mater. Sci. Eng. A* 293, 81–87.
- Rice, J.R., 1988. Elastic fracture mechanics concepts for interfacial cracks. *J. Appl. Mech.* 55 (1), 98–103.
- Shaw, M.C., Marshall, D.B., Dadkhah, M.S., Evans, A.G., 1993. Cracking and damage mechanisms in ceramic/metal multilayers. *Acta Metall. Mater.* 41 (11), 3311–3322.
- Shi, Z.L., Yang, J.M., Lee, J.C., Zhang, D., Lee, H.I., Wu, R.J., 2001. The interfacial characterization of oxidized SiCp/2014 Al composites. *Mater. Sci. Eng. A* 303, 46–53.
- Somerday, B.P., Leng, L., Gangloff, R.P., 1995. Elevated temperature fracture of particulate-reinforced aluminum. Part I: Fracture toughness. *Fatigue Fract. Eng. Mater. Struct.* 18, 565–582.
- Tada, H., Paris, P., Irwin, G., 1973. *The Stress Analysis of Cracks Handbook*. Del Research Corporation, Hellertown, PA, p. 2.10.

- Tjong, S.C., Ma, Z.Y., 2000. Microstructural and mechanical characteristics of in situ metal matrix composites. *Mater. Sci. Eng. R: Rep.* 29, 49–113.
- Wang, C.K., Huang, Q.G., 1996. Tensile properties of LF6 aluminum alloy at high temperature. In: *National Conference on the Thermal and Mechanical Effect of Materials Induced by Laser Beam* (in Chinese). Ningbo, Zhejiang, pp. 202–206.
- Wang, R., Huang, K.Z., Zhu, Z.X., 1988. *Advance in Plastic Mechanics*. Chinese Railway Press, pp. 119–143.
- Wilner, B., 1988. Stress analysis of particles in metals. *J. Mech. Phys. Solids* 36, 141–165.
- Wu, X.R., 1984. Approximate weight functions for center and edge cracks in finite bodies. *Eng. Fract. Mech.* 20, 35–49.
- Zhou, Y.C., Duan, Z.P., Xie, B.M., 1997. Long pulsed laser induced reverse bulging and plugging. *Int. J. Eng. Sci.* 35, 613–621.
- Zhou, Y.C., Duan, Z.P., Yang, Q.B., 1999. A thermal-elastic analysis on laser-induced reverse bulging and plugging in circular brass foil. *Int. J. Solids Struct.* 36, 363–389.
- Zhou, Y.C., Long, S.G., Duan, Z.P., Hashida, T., 2001a. Thermal damage and fracture of particulate-reinforced metal matrix composites induced by laser beam. *Trans. ASME J. Eng. Mater. Technol.* 123 (3), 251–260.
- Zhou, Y.C., Zhu, Z., Duan, Z.P., 2001b. Thermal fracture characterizations induced by laser beam. *Int. J. Solids Struct.* 38 (32–33), 5647–5660.